Parametric aeroelastic modeling, maneuver loads analysis using CFD methods and structural design of a fighter aircraft

A. Voß *, T. Klimmek

DLR - German Aerospace Center, Göttingen, Germany

ARTICLE INFO

ABSTRACT

The DLR Future Fighter Demonstrator (FFD) is a highly agile, two-seated aircraft with twin-engines equipped, a reheat and a design flight speed extending into the supersonic regime (up to $Ma = 2.0$). Based on a given conceptual design, the presented work focuses on the aeroelastic modeling, including structures, masses and aerodynamics. Using the models, a comprehensive loads analysis with 688 maneuver load cases, covering the whole flight envelope, is performed. Comparing the results obtained from aerodynamic panel methods (VLM and ZONA51) with higher fidelity results obtained from CFD, the necessity of CFD based maneuver loads analysis in preliminary design of such fighter configuration is shown, as it leads to physically different as well as higher loads. The rigorous application of CFD is a heavy burden during the preliminary design, but this work demonstrates that it is doable as of today. Finally, the model is subject to structural optimization, demonstrating that the differences in loads result in a heavier primary structural net mass with ≈ 3.3 t for the approach based on aerodynamic panel methods and ≈ 4.1 t for the CFD based approach. Because all remaining models are unchanged, this difference in mass can be clearly attributed to the physical differences in the flow solutions obtained from the panel methods and CFD.

1. Introduction and motivation

1.1. Objectives

Within a DLR-internal project, a conceptual design of a fighter aircraft is developed. In this work, we focus on the aeroelastic modeling and the loads analysis followed by a structural sizing. These analyses are enabled by application of a parametric modeling process already at an early stage of the design. Because the design flight envelope extends into the supersonic range, special attention needs to be put on the aerodynamic methods. For the subsonic load cases, the vortex lattice method (VLM) is used while for the load cases with $Ma > 1.0$, a supersonic aerodynamic panel method (ZONA51) is employed. Both methods were compared in [1] to higher fidelity results obtained from CFD to assess their validity and/or possible shortfalls. It became clear that panel methods are at their physical limit and that in particular for fighter aircraft, CFD should be preferred over panel methods. With this understanding, the presented publication focuses on CFD maneu-

ver loads (based on the trimmed aircraft, coupled with the elastic structure, including control surface deflections, for 688 load cases, in all areas of the flight envelope) as a consequent extension to [1]. The rigorous application of CFD is a heavy burden in terms of computational cost during the preliminary design, but this publication demonstrates that it is doable as of today. In addition, CFD requires a high quality outer geometry, leading to an extension of the existing model generation software. The CFD-based results are compared to the ones based on the panel methods in terms of section loads at different monitoring stations to evaluate the differences of the load envelopes. Finally, the differences in loads are illustrated in terms of material thickness using a structural optimization, resulting in a heavier primary structural mass. Knowing the differences is important because aerodynamic panel methods are an important tool in preliminary aircraft design.

1.2. The DLR future fighter demonstrator

The DLR Future Fighter Demonstrator (FFD) is a highly agile, two-seated aircraft with twin-engines with reheat and a targeted maximum take-off mass between 30.0 and 36.0 t. An overview of the key parameters is given in Table 1. Within the project, the DLR Institute of System Architectures in Aeronautics has taken the task to devise a conceptual design that fulfills the top level air-

* Corresponding author.
  E-mail addresses: arne.voss@dlr.de (A. Voß), thomas.klimmek@dlr.de (T. Klimmek).

Table 1

Overview of DLR Future Fighter Demonstrator (FFD) key design parameters.

| Property	Parameter / Description
Maximum speed	$VC = Ma$ 2.0 at 36,000...50,000 ft $VD = Ma$ 2.3 at 36,000...50,000 ft
Maximum altitude	50,000 ft
Mission radius	550...700 NM
Mass	30.0...36.0 t maximum take-off mass (MTOM)
Payload	air 2 air mission: 1820 kg (internal) optional: 8000 kg (internal + external)
Agility	Load factor $Nz = -3.0 \cdots +9.0$ with basic flight design mass (BFDM)
Longitudinal Stability	Subsonic: unstable, supersonic: stable
Control surfaces	All-movable horizontal tail planes (pitch) Vertical tail planes with rudder (yaw) Ailerons along the main wing trailing edge (roll)
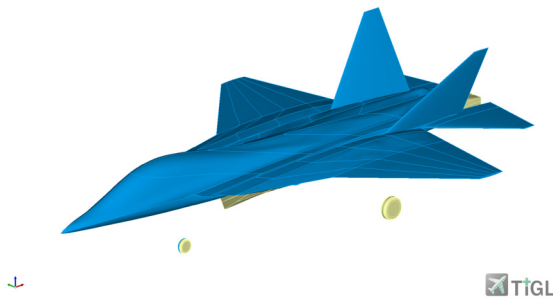
Fig. 1. The DLR Future Fighter Demonstrator (FFD), CPACS file visualized in the TiGL Viewer.

craft requirements (TLARs) which were defined beforehand in a project-internal specification document. A special software and a knowledge based approach is used that relies on empirical correlations from a multitude of disciplines. They are combined with an automated constraint and mission capability analysis. More details on that approach are given by Mancini et al. [2]. The resulting conceptual design is then enhanced with a more detailed aerodynamic shape [3] in a manual step by the DLR Institute of Aerodynamics and Flow Technology. The resulting geometry of the FFD is shown in Fig. 1. In parallel, an engine is designed by the DLR Institute of Propulsion Technology. To enable the exchange of information within the project, the Common Parametric Aircraft Configuration Schema (CPACS) [4] is used.

1.3. Literature review

For civil configurations, a lot of knowledge on loads analysis and structural sizing exists and, correspondingly, a significant number of publications are available. Some selected DLR publications are by Schulze et al. [5] with a focus on an optimal load adaptive wing and by Klimmek et al. [6] with a focus on the integration into a multidisciplinary optimization chain. Handojo [7] investigated the influence of loads alleviation and fatigue and Sinha et al. [8] concentrated on the composite material modeling. Unconventional configurations, such as flying wings, are studied by Voß [9], Hecken et al. [10] investigated on cargo drones and Voß et al. [11,12] performed the loads analysis for a high altitude, long endurance configuration. Most aircraft companies have developed their own methods and tools, but literature is rarely available. Lockheed developed the L-1011 TriStar using computational methods for loads analysis, as reported by Stauffer et al. [13,14]. Next to Lockheed, work was also done at Boeing, e.g. by D'Vari and Baker [15] presenting an aeroelastic integrated loads subsystem. A framework used at Airbus and DLR is VarLoads, literature can be found by Kier et al. [16,17] or Scharpenberg et al. [18]. The software used

in this work is the Loads Kernel, which is a DLR in-house tool. The theoretical background is documented in [19,20].

Considering that most of the development work of military configurations is confidential, a surprisingly large number of contributions with in-depth information on loads requirements can be found in two comprehensive resources [21,22] published by the NATO Research and Technology Organization (RTO) and the NATO Advisory Group for Aerospace Research and Development (AGARD). For example, Petiau [23] gives some background on the philosophy of design loads at Dassault (w.r.t. Dassault's Mirage and Rafale). Neubauer and Günther [24] give a general overview on the strategy for loads analyses at Airbus Defense and Space (w.r.t. Tornado and Eurofighter). Watson [25], from British Aerospace, gives details on the structural design criteria with a detailed discussion on dimensioning load cases (w.r.t. Eurofighter). Luber et al. [26] discuss the impact of different dynamic loads on an aircraft design and give details on the calculation procedures (w.r.t. Eurofighter). Molkenthin [27] explains how Airbus tries to develop so-called standardized maneuvers, which can be derived from actual operational maneuvers that are practiced by pilots to achieve a specific motion of the aircraft. From these standardized maneuvers, operational flight loads can be derived as shown by Struck and Perron [28].

Finally, a general framework of conditions for military aircraft is defined in MIL-A-8860B [29] and MIL-A-8861B [30], which follows a similar approach compared to CS-25 [31].

The literature mentioned above gives a deep insight into industrial practice and shows that the loads analysis is an essential part in the course of the development process of a new aircraft. To the author's best knowledge, CFD based maneuver loads haven't been demonstrated and/or published before for a fighter configuration and not at the scale as shown in this work.

2. Parametric aeroelastic modeling

2.1. Parametric geometrical modeling

For the set-up of the aeroelastic simulation models, namely the structural model, the mass models for the primary structure and the fuel, the aerodynamic model, and the aero-structural coupling model, the parametric model generator ModGen [32] is used, which is developed at the DLR Institute of Aeroelasticity. For this work, various geometry-related features are developed and implemented into ModGen with the aim to derive the basic outer geometry directly from the CPACS dataset, which is set-up during the conceptual design of the DLR Future Fighter Demonstrator (FFD). Note that in previous ModGen applications, the outer geometry was defined by internal ModGen specific parameters and input conventions. To deal with the outer geometry defined by

CPACS for the FFD configuration, the parametric geometrical functions (mainly B spline functions representing curves and surfaces), are set-up within ModGen, similar to DLR's TiGL functions [33]. This concept ensures that the outer geometry is as close as possible to the geometry defined by the CPACS dataset. Then, ModGen's internal geometry processing capabilities are applied for the set-up of geometry models for the primary structure parts like spars and ribs, see Section 2.2, and to create an outer hull for CFD mesh generation, see Section 2.4. For a smooth wing-fuselage geometry, the wing and the fuselage are defined in CPACS as one wing running from left to right and are partitioned into segments. To ensure at least C2 and in part C0 continuity between the segments, so-called guiding curves are defined for the complete wing and fuselage geometry, which are shown in Fig. 2a. The use of guiding curves leads to a segment wise definition of the outer geometry with so-called Gordon surfaces [34]. Gordon surfaces are created by interpolating a proper curve network, where the intersection points between the curves are known. Gordon surfaces are different from tensor product splines, that are a collection of various polynomial surfaces which are connected with distinct continuity.

The blending surface interpolates the $n \times m$ curve network $\mathbf{f}_i(u)$ and $\mathbf{g}_j(v)$ for the parametric directions u and v and the blending functions $\Psi_i(v)$ and $\Phi_j(u)$:

$$
\begin{aligned}
\mathbf{s}(u,v) = &\sum_{i=1}^{n} \mathbf{f}_i(u)\Psi_i(v) \\
&+ \sum_{j=1}^{m} \mathbf{g}_j(v)\Phi_j(u) \\
&- \sum_{i=1}^{n}\sum_{j=1}^{m} \mathbf{p}_{i,j}\Phi_j(u)\Psi_i(v)
\end{aligned}
\tag{1}
$$

with the intersection points $\mathbf{p}_{i,j}$ between n curves $\mathbf{f}$ and the m curves $\mathbf{g}$. Rewriting eq. (1) leads to

$$
\mathbf{s}(u,v) = \mathbf{s}_f(u,v) + \mathbf{s}_g(u,v) - \mathbf{t}(u,v)
\tag{2}
$$

where $\mathbf{s}_f(u,v)$ and $\mathbf{s}_g(u,v)$ represent the individual spline interpolation for the curve families $\mathbf{f}$ and $\mathbf{g}$. The surface $\mathbf{t}(\mathbf{u},\mathbf{v})$ is a so-called tensor product surface using the intersection points $\mathbf{p}_{i,j}$ and the blending functions $\Psi_i(v)$ and $\Phi_j(u)$. In order to make the formula for $\mathbf{s}$ applicable for the profile curves and the guide curves of the FFD configuration, which represent the two curve families $\mathbf{f}$ and $\mathbf{g}$, several steps to harmonize the parameterization of the curves have to be done. The potential different parametrization of even the curves is basically rooted in the fact that each curve is individually defined to fit best for the target geometry. As far as B-splines were chosen for the parametric curves and surfaces, the curves within its family have to have the same knot set and order and for the superposition together with the blending functions $\Psi_i(v)$ and $\Phi_j(u)$, the surfaces $\mathbf{s}_f(u,v)$, $\mathbf{s}_g(u,v)$ and $\mathbf{t}(u,v)$ have to be compatible (same knot set and same order of and parametric directions) as well, such that all three surfaces can be superposed to $\mathbf{s}(u,v)$. A formal and exact harmonization would lead to a surface definition with a massive number of parameters and high order. Therefore, in a first step, each surface $\mathbf{s}_f(u,v)$, $\mathbf{s}_g(u,v)$ and $\mathbf{t}(u,v)$ is set-up individually after harmonizing the curves. Then, in the second step, the surfaces are re-parametrized by extracting proper numbers of curves and splining them again to obtain $\widetilde{\mathbf{s}}_f(u,v)$, $\widetilde{\mathbf{s}}_g(u,v)$ and $\widetilde{\mathbf{t}}(u,v)$. Now, the number $\widetilde{n}$ and $\widetilde{m}$ of the curves per surface and the knot set and order of the curves are defined in a coordinated way such that the superposition yields $\widetilde{\mathbf{s}}(u,v)$. For the definition of the internal load carrying structure, like spars and ribs, a classical definition convention with

(a) Processing of the outer geometry using guiding curves

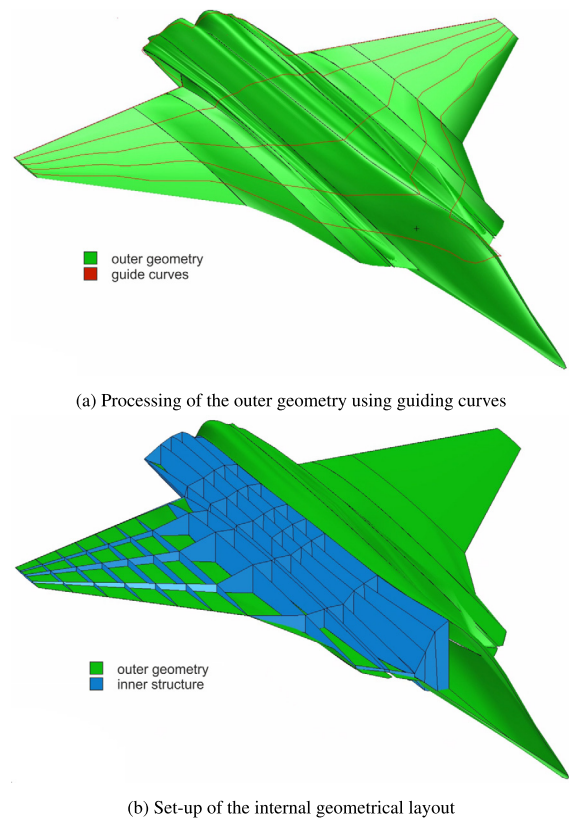(b) Set-up of the internal geometrical layout

Fig. 2. Geometry processing with ModGen for the DLR Future Fighter Demonstrator (FFD). (For interpretation of the colors in the figure(s), the reader is referred to the web version of this article.)

respect to the number, position, and orientation, is applied, resulting in a internal structural layout shown in Fig. 2b in blue color. Together with the upper and lower skin, this internal geometrical layout provides the baseline for the set-up of the grids and finite element models, which are described in the following Sections.

2.2. Structural model

The first aim of the structural model is to adequately represent the overall structural dynamic characteristics of the aircraft in terms of frequencies and mode shapes, which are important for aeroelastic analyses. Second, the model shall provide a baseline for the structural sizing, which is described in Section 5. Therefore, all primary structural elements, including the spars, ribs, upper and lower skin, are modeled using shell elements (CQUAD4, PSHELL and MAT1) and are completed by spar caps, stiffeners and stringers, using beam elements, to avoid local buckling and to provide a more realistic structure. For the wing, a structural layout with three main spars and multiple ribs, orientated in flow direction, is devised, see Fig. 3. From an ideal structure point of view, the main spars would continue up to the center line of the aircraft, providing a good load path and high second area moments to take the wing root bending moments. However, the majority of the available space in the fuselage region is taken up by the twin-engines and their air intakes. Most of the remaining space is required for the weapon and landing gear bays as well as for fuel tanks. Thus, the main spars are discontinued and the "hollow" fuselage region is bridged by standard I-beam (alternative names: double T- or H-beam) elements (CBAR, PBARL and MAT1) located on the top and bottom, providing sufficient space for the engines, air intake, etc. in between. Note that the beam elements are representative simplifications of the stiffening structural elements and
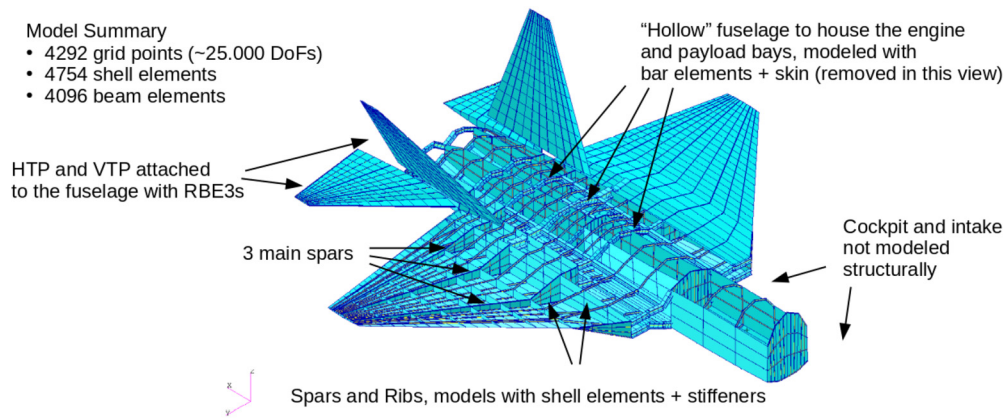
Fig. 3. Structural modeling using finite elements.

should be replaced by a more detailed finite element modeling using shell elements in future design phases. Because the beam's cross sections are included in the sizing, see Section 5, they provide a good estimate in terms of required cross section and second area moment. Similar to the wing, the horizontal and the vertical tail are modeled and attached to the rear fuselage using interpolation elements (RBE3). Not included in the structural model are the air intakes and the cockpit. The rational behind this decision is that although both components are large, they don't belong to the primary, load-carrying structure and their influence on the overall structural dynamic behavior of the aircraft is neglected though their mass and moment of inertia is considered. Future developments aim at including the support structure of these components as well to increase the fidelity of the modeling. The resulting MSC.Nastran finite elements model is shown in Fig. 3, has a size of 25.000 degrees of freedom (DoF) and includes 4292 grid points, 4754 shell elements and 4096 beam elements.

2.3. Mass model

For loads analysis it is important that the mass model is as complete as possible and that the masses are distributed over the aircraft at their actual location, because both has a significant impact on the section loads. The mass model includes the structural masses, system masses, fuel masses and payload. The structural masses are derived from the skin thickness and/or the cross section of the beam elements combined with the material density. Note that when the material thickness changes during the sizing, this has an influence on the structural weight. The structural masses are completed by mass estimates for the components not included in the structural model (e.g. air intakes and cockpit). For the aircraft systems, empirical mass estimates are available from the conceptual design. Also, a total of 9909 kg of fuel is estimated, which is distributed over four fuel tanks per side as shown in Fig. 4. The fuel is then modeled with volume elements and MSC.Nastran is used to calculate both mass and inertia properties. Finally, a design payload of 1820 kg for an air to air mission is taken into account, distributed over three weapon bays. To combine the structural stiffness and mass model, an approach with one condensed mass per sub-section is used. One sub-section is described for example by two ribs, two spars and the enclosed skins. The individual masses are condensed at the center of each sub-section using a nearest-neighbor approach, the inertia properties are maintained. The center grid points are connected to the corner points of each sub-section using interpolation elements, so that the inertia forces will be introduced into the structure smoothly without creating undesired local stress peaks. Different combinations of fuel and payload masses are considered using four mass config-

Table 2
Overview of mass configurations.

Mass case	Fuel	Payload	Mass
M1 (MTOM)	100%	Yes	26.2 t
M2 (BFDM)	70%	Yes	23.2 t
M3	70%	No	21.4 t
M4 (OEM)	0%	No	14.5 t

urations summarized in Table 2 and shown in Fig. 5. The configurations M1 to M4 are selected in such a way that they roughly represent the different mass cases that occur during a mission of the aircraft, ranging from the heaviest mass case M1 at take-off to the lightest mass case M4 just before landing. Mass case M2 corresponds to the basic flight design mass (BFDM) where the aircraft is required to achieve its full performance. Mass case M3 is similar to M2 but without payload.

2.4. Aerodynamic models for panel and CFD methods

To obtain aerodynamic pressure distributions, the vortex lattice method (VLM) [20] is used for the subsonic regime and the ZONA51 method [35,36] for the supersonic regime. For both methods, the lifting surfaces are discretized using a panel mesh (1112 panels) shown in Fig. 6. The left and right horizontal tail planes (HTP) are all-movable and are used for pitch control while the left and right vertical tail planes (VTP) have a conventional rudder. Ailerons are located along the trailing edge of the main wing. Although the aerodynamic methods consider the lifting surfaces as flat plates, it is possible to add a correction for airfoil camber and wing twist, which is indicated by the color in Fig. 6. Note that currently a (preliminary) symmetric airfoil is used for the wings, so the main influence of this correction can only be seen in the fuselage region.

Following Watson [25], linear aerodynamics are adequate for calculating design loads, as the highest loads typically arise at high-speed conditions where the aerodynamics remain within their linear regime. To assess their validity and/or possible shortfalls, both aerodynamic panel methods are compared with higher fidelity results obtained from CFD in Section 3. Considering that for loads analyses, capturing all major physical effects adequately (but not precisely or to the last detail as an aerodynamic specialist would prefer) is important, the authors believe that the Euler equations are a reasonable choice when comparing computational cost and precision of the results. This assumption is justified in the next section. From Probert's overview on wing design of combat aircraft [37], it can be concluded that much of the aerodynamic design work for the Tornado and the Eurofighter was performed using Euler codes. In this work, the DLR Tau [38] code and the SU2
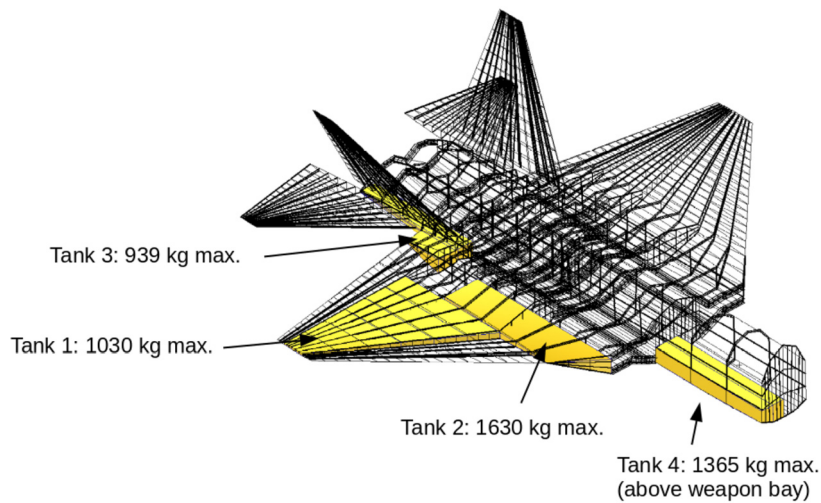
Fig. 4. Fuel modeling using volume elements to estimate mass and inertia properties.
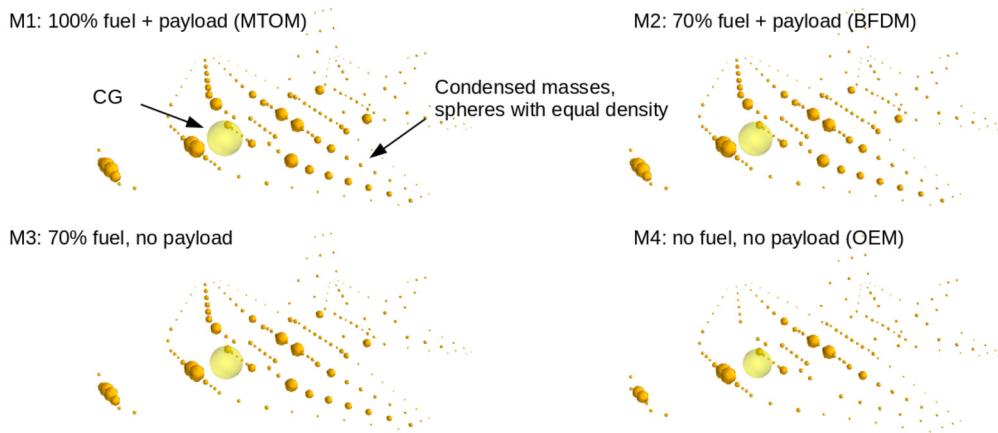

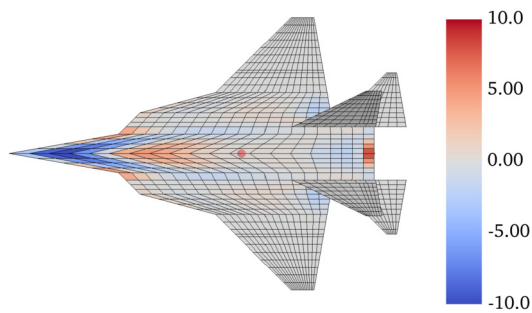**Fig. 5.** Mass modeling with condensed masses and four mass cases.

Fig. 6. Aerodynamic mesh for VLM & ZONA51 incl. correction for camber and twist (indicated by color).

[39] code are used. The underlying aerodynamic mesh is generated based on the outer geometry generated with ModGen, which in turn relies on a CPACS dataset as described in Section 2.1. The HTP and VTP geometries are blended with the main aircraft using Siemens Simcenter 3D [40]. The meshing is performed using the mesh generator Centaur [41] and results in a surface mesh with 206k triangles as shown in Fig. 7a. Because no boundary layer is required for Euler solutions, tetrahedrons can be used directly to fill a spherical control volume. To better resolve vortices, which are expected to appear already at low angles of attack and get more intense towards higher angles of attack, the volume mesh is refined in proximity to the aircraft using a conical frustum, visual-

ized in Fig. 7b. This results in a mesh with a total number of 4.4M volume cells and 0.8M volume points. Note that the same aerodynamic mesh is used for both flow solvers, the only difference is the conversion into the native mesh format of each CFD solver.

3. Comparison of panel aerodynamics with CFD

In a first step, three different CFD solutions are compared. The Tau Euler and the SU2 Euler solutions are prepared using the mesh described in Section 2.4 while the Tau RANS solutions [3] are provided by the DLR Institute of Aerodynamics and Flow Technology, for which the authors are very thankful. Fig. 8 shows a visualization of the vortices using the Q-criterion [42,43] with iso-surfaces at $Q = 50$ for a representative low-speed operational point at $Ma = 0.4$ and $\alpha = 15.0°$. Two primary vortices can be identified in all three solutions, one starting at the strake and one starting at the leading edge of the main wing. In general, the vortices appear to be slightly stronger in the two Euler solutions compared to the RANS solutions, which is as expected due to the missing viscous dissipation. The surface pressure distributions c_p shown in Fig. 9 are very similar in all three solutions, too. The "footprints" of the vortices are visible as suction peaks in green to blue colors. From the loads analysis perspective, the Euler equations are a reasonable choice for the FFD configuration with respect to computational cost, precision and geometric model requirements and are used for all following analyses.
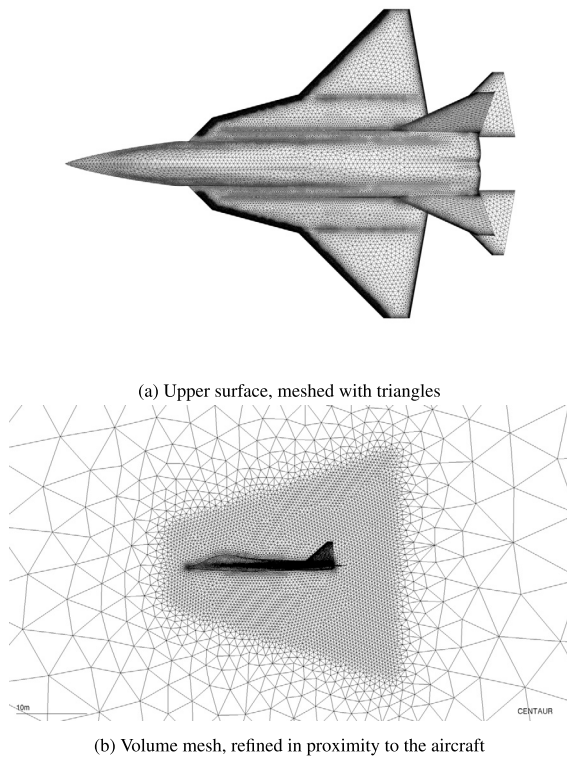
(a) Upper surface, meshed with triangles

(b) Volume mesh, refined in proximity to the aircraft

Fig. 7. Aerodynamic mesh for CFD solution.

In a next step, the CFD solutions are compared to the vortex lattice method (VLM). The VLM [20] is based on a matrix of aerodynamic influence coefficients, the so-called **AIC**, which only depends on the Mach number Ma and the geometry of the aircraft. The **AIC** matrix then relates an induced downwash $\mathbf{w}_j$ on each aerodynamic panel to a pressure coefficient

$$\Delta\mathbf{c_p}^{\text{AIC}} = \mathbf{AIC}(Ma) \cdot \mathbf{w}_j \quad . \tag{3}$$

This means that the VLM scales purely linear with for example the angle of attack. Because the VLM assumes a flat plate, the pressure coefficient $\Delta\mathbf{c_p}^{\text{AIC}}$ yields the pressure difference between upper and lower side. Thus, a comparison with CFD is not straightforward and requires at first a split of the volumetric body of the CFD solution in an upper and lower side (remove the VTP). Then the surface pressure values are projected onto xy-plane and interpolated at the panel centers of the VLM mesh. Finally, a pressure difference between upper and lower side is calculated with

$$\Delta c_p^{\text{CFD, interp}} = c_{p,\text{lower}}^{\text{CFD, interp}} - c_{p,\text{upper}}^{\text{CFD, interp}} \quad . \tag{4}$$

Fig. 10 shows the pressure coefficient distribution $\Delta\mathbf{c_p}$ for the low-speed operational point at $Ma = 0.4$ and $\alpha = 15.0°$. For the CFD solution, the vortices are clearly visible in the pressure coefficient distribution. However, the VLM solution only shows a suction peak along the leading edge but the vortices are not captured. This is as expected due to the linear approach of the VLM, but leads to a significantly different aerodynamic loading in both span and chord direction. Finally, the VLM uses a Prandtl-Glauert transformation with $\beta = \sqrt{(1 - Ma^2)}$ to account for compressibility. This approach is limited in the transonic regime and becomes singular close to $Ma = 1.0$.

Fig. 11 shows the pressure coefficient distribution $\Delta\mathbf{c_p}$ for a representative high-speed operational point at $Ma = 1.4$ and $\alpha = 5.0°$. In the supersonic regime, the angle of the compression wave front is given by $\mu = sin^{-1}(1/Ma)$ with $\mu = 45.6°$ for Ma=1.4. The

compression shocks result in a jump of the surface pressure distribution. Like in the subsonic regime, vortices are also present in the supersonic regime, making a direct comparison of the pressure distributions between CFD and ZONA51 difficult. Still, compression shocks can be identified in both solutions and at the same locations as indicated by the dashed lines.

The two comparisons in the sub- and supersonic regime between CFD and the panel methods show only a moderate agreement. Still, because section loads are very integral quantities, the overall influence on the preliminary sizing might be less pronounced. Apart from that, the panel methods are clearly at their physical limit for fighter aircraft, indicating that CFD should be preferred over panel methods. However, CFD maneuver loads (based on the trimmed aircraft, coupled with the elastic structure, including control surface deflections, for 688 load cases, in all areas of the flight envelope) mean a significant increase of the needed effort on both the modeling and the computational side.

4. Loads analysis

4.1. Load case selection

There are a large variety of steady and dynamic load cases that have an influence on the design of an aircraft, e.g. dynamic gust encounter, buffet loads on the rear of the aircraft, gunfire loads at attachment points, so-called hammershock loads at the air intake, bird strike, jettison, landing loads, ground loads, etc. (compare with Luber et al. [26]). Because each type of load case requires a special analysis and in several cases also data from experimental measurements, taking everything into account is not feasible for an early preliminary design stage. In addition, most of the load cases mentioned above are only relevant for a specific part of the aircraft. Based on their experience with civil transport aircraft, the authors of this work assume that for the sizing of the primary aircraft structure, both maneuver and gust loads are potential driving factors. More elaborate load analysis may be added at later stage during the design process. As a simplified and conservative means to estimate gust loads, the Pratt formula [44,45] allows to translate a gust encounter into an equivalent load factor N_z. For the FFD configuration, the highest Pratt load factor obtained was $N_z \leq 3.0$, which is much lower than the maximum load factor $N_{z,\text{max}} = 9.0$ from the maneuver load cases, which are caused by the high maneuverabilty requirements. Knowing that the Pratt formula is designed for classical transport and not for fighter aircraft, the authors still believe that the results are at least representative. Consequently, gust loads can be ruled out for the sizing of the primary, load-carrying structure of this aircraft. Note that a gust encounter could still be important, for example a short gust encounter might lead to high local accelerations at the wing tip, which might be dimensioning for under-wing attachment points, see Luber et al. [26].

Concerning maneuver load cases, time domain simulations with cockpit control displacements as given e.g. in MIL-A-8861B [30] are not doable during the preliminary design phase, because this would involve an electronic flight control system (EFCS) which is not yet available at this stage of the design process. Also, because no measurements or flight test data are available, operational flight loads are neither an option. Thus, a number of representative design load cases are derived from the aircraft requirements. This is a pragmatic approach for the preliminary design and is also used e.g. at Dassault as stated by Petiau [23] and for the Eurofighter as explained by Watson [25]. The task of the EFCS is then to ensure that the aircraft stays within the boundaries set by the design load cases. Should more detailed knowledge and/or the flight test reveal the assumptions were too conservative, the additional margin can be used by the EFCS for the benefit of better flying and handling
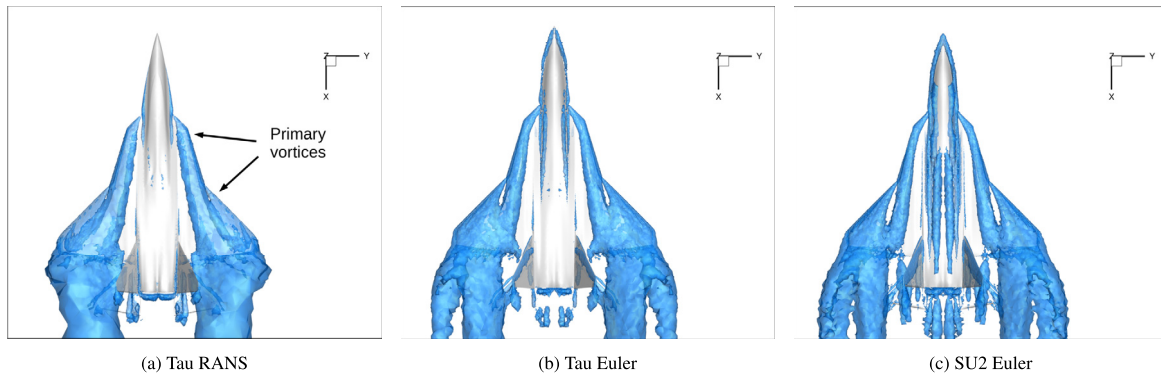
(a) Tau RANS　　　　　　　　(b) Tau Euler　　　　　　　　(c) SU2 Euler

Fig. 8. Visualization of the vortices using the Q-Criterion at $Ma = 0.4$ and $\alpha = 15.0°$.

(a) Tau RANS　　　　　　　　(b) Tau Euler　　　　　　　　(c) SU2 Euler
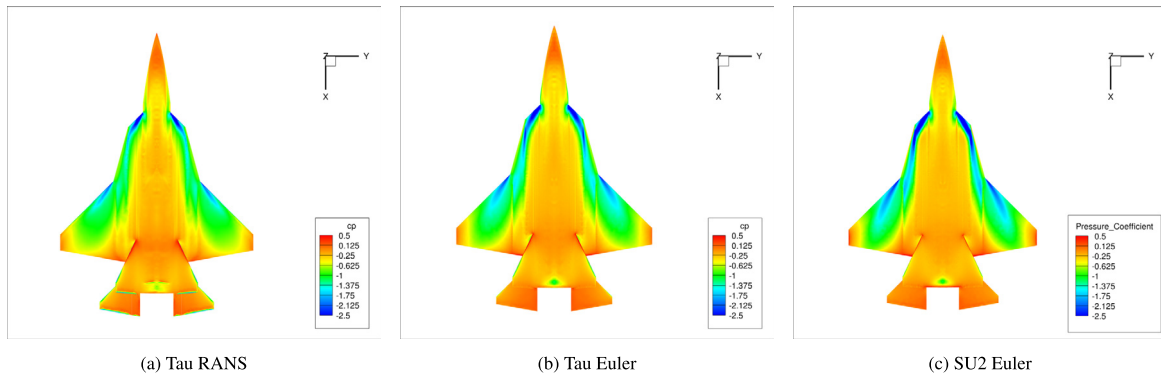
Fig. 9. Surface pressure distribution c_p at $Ma = 0.4$ and $\alpha = 15.0°$.
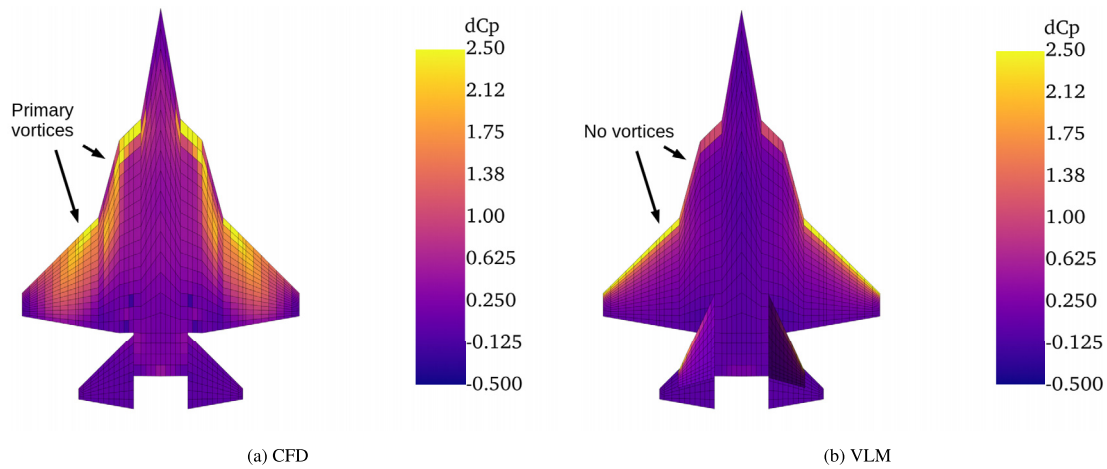

(a) CFD　　　　　　　　　　　　　　　　(b) VLM

Fig. 10. Pressure coefficient distributions Δc_p at $Ma = 0.4$ and $\alpha = 15.0°$.

qualities. The flight envelope of military aircraft shown in Fig. 12 and defined in MIL-A-8860B [29] and MIL-A-8861B [30] follows a similar approach compared to the flight envelope of civil aircraft defined for example in CS-25 [31]. In this work, the military flight speeds V are indicated with a subscript and the civil flight speeds with a capital character. For example, the level flight maximum speed V_H corresponds to the design cruising speed VC, the limit speed V_L corresponds to the design dive speed VD and the minimum speed V_e at which the design limit load factor can be attained corresponds to the design maneuvering speed VA. The left side of the flight envelope is completed by the stall speeds V_S and VS, which exists in both military and civil specifications. Note that the military specification asks for a reduction of V_S and V_e by a factor $K = 1.0 \ldots 1.25$ for flight speed below Ma=1.0 to account for

buffet loads, which are given in Fig. 12 by the dashed gray lines. On the aerodynamic side, this would require higher lift coefficients than physically achievable, which is mathematically possible with linear panel methods but can't be achieved using more physical methods such as CFD. Thus, for this work, the authors decided against using the reduction factor K.

The maneuver load cases include pull-up and push-down maneuvers with a load factor $N_z = -3.0 \ldots 9.0$. Both pull-up and push-down maneuvers are combined with maximum elevator commands in opposite direction, which reflects a sudden change of mind by the pilot. Steady roll maneuvers with constant roll rates p as well as accelerated roll maneuvers with $\dot{p}$ in opposite direction are considered for horizontal level flight and in combination with the pull-up and push-down maneuvers. Depending on the flight
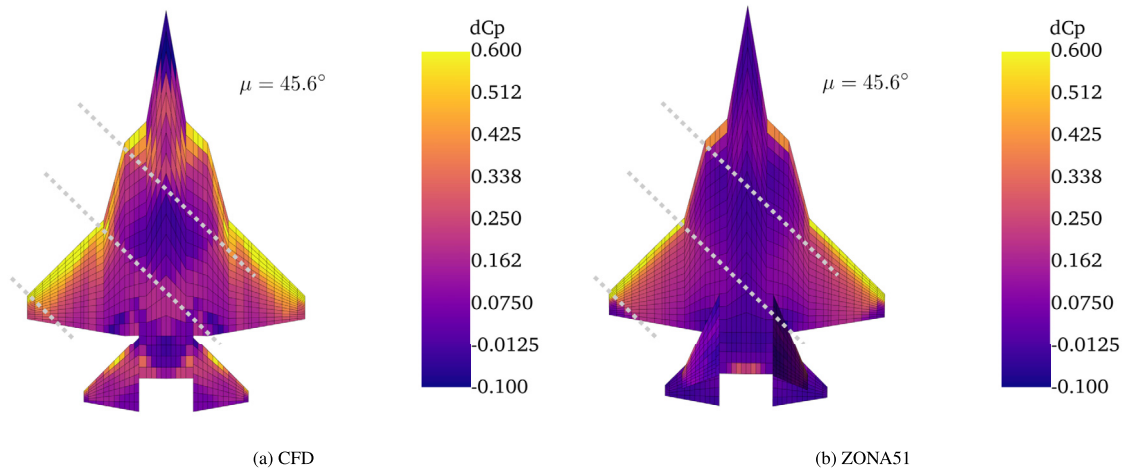
(a) CFD

(b) ZONA51

Fig. 11. Pressure coefficient distributions Δc_p at $Ma = 1.4$ and $\alpha = 5.0°$.

Table 3
Overview on maneuver load parameters.

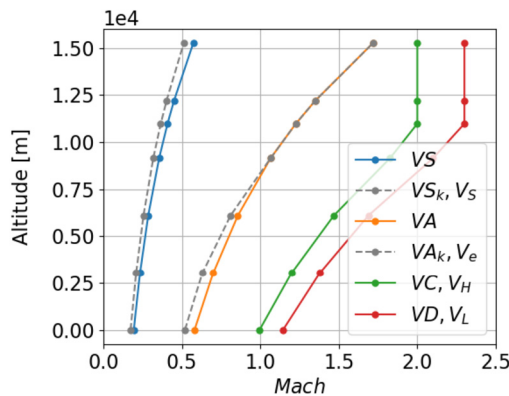| Maneuver load parameters	Value / Range
Load factor N_z	$N_z = -3.0 \ldots 9.0$
Roll rate p	$p = \pm 20°/s \cdots \pm 220°/s$
Roll acceleration $\dot{p}$	$\dot{p} = 20°/s^2 \ldots 550°/s^2$
Elevator deflection η	$\eta_{min,max} = \pm 15°$

Fig. 12. Proposed design speeds.

speed and angle of attack, the roll rate p ranges from $25°/s$ for low speed and high angle of attack to $220°/s$ for higher speed and low angles of attack. In a similar way but with a larger spread, the roll acceleration $\dot{p}$ changes from $\dot{p} = 20°/s^2 \ldots 550°/s^2$. A summary of all parameters is given in Table 3. The maneuver load cases are considered for all flight speeds and at seven different altitudes with an interval of 10 000 ft (every dot in Fig. 12 indicates an operational point) because as Neubauer and Günther [24] point out, it is important to consider not only the corner points of the flight envelope but also operational points within the envelope. The reason is that the interaction of aerodynamics, the flexible structure and control surface deflections is difficult to predict analytically. Also, all four mass configurations M1 to M4 are considered, but not in combination with all maneuver cases because for example the maximum load factor $N_{z,max}$ only has to be reached for M2 (BFDM) but not for M1 (MTOM). As most operational points are above $Ma = 1.0$, this results in a total number of 175 subsonic and 513 supersonic maneuver load cases.

4.2. Load envelopes

The resulting loads are evaluated in terms of section loads at so-called monitoring stations. Fig. 13 shows an example of a two-dimensional envelope of the bending moment M_x and the torsional moment M_y for a monitoring station located at the right wing root. Every dot corresponds to one maneuver load case and the subsonic load cases are plotted in blue while the supersonic cases are plotted in green color. Because the underlying mass and structural models are the same, all difference described below can be clearly attributed to the differences in the aerodynamics as discussed in Section 3.

From both Figs. 13a and 13b, it is evident that the highest bending and torsional moments identified by the merged load envelope (black and gray) are similar. The minimum and maximum bending moments are $M_{x,min} \approx -0.7 \cdot 10^6$ Nm and $M_{x,max} \approx +1.8 \cdot 10^6$ Nm, while the minimum and maximum torsional moments are $M_{y,min} \approx -0.75 \cdot 10^6$ Nm and $M_{y,max} \approx +1.1 \cdot 10^6$ Nm for both the CFD and the panel method based loads. Looking closer, it becomes clear that for example in Fig. 13a the lower right corner of the envelope is dominated by subsonic load cases (blue) while in Fig. 13b, the lower right corner is defined by supersonic load cases (green). The upper right corner also looks different; for the CFD maneuver loads, the maximum torsional moment M_y comes with a much higher bending moment M_x compared to the panel method loads, where the upper right corner is dented / pushed to the left. Generally speaking, in Fig. 13b the supersonic envelope (green) is rotated in clock-wise direction with respect to the subsonic envelope (blue). This could be explained by the large range of travel of the aerodynamic center, with a location further rearwards for supersonic speeds compared to subsonic speeds. However, this effect is not visible for the CFD maneuver loads in Fig. 13a.

Looking deeper into the details, it is surprising to see that the corners of the envelopes are mostly defined by the same maneuvers load cases, which are identified by their numbers. For example, starting at the top and proceeding in clock-wise direction, the load cases with number 10071, 10077, 10072, 10091, 10074, 10080, 10073 and 10092 define the envelope for the subsonic maneuvers (blue). The same is true for the supersonic maneuvers (green), here the load cases with numbers 20333, 20295, 20301, 20296, 20315, 20298, 20342, 20304, 20303, 20297 lie on the envelope. There are only small differences, for example on the left side of the supersonic envelope, load case number 20019 is identified instead of 20076. So for this configuration, an approach to save computation time could be to identify the important load cases using panel methods first and use CFD only for the reduced set of
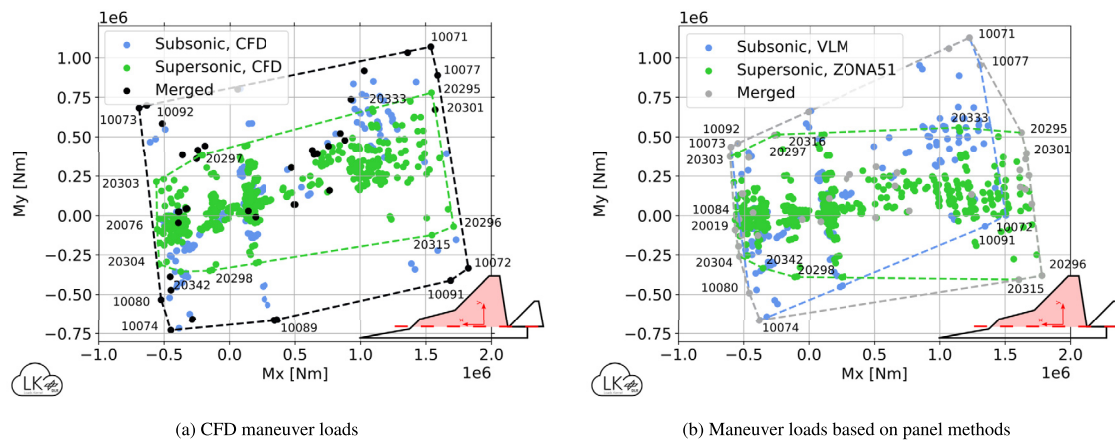
(a) CFD maneuver loads

(b) Maneuver loads based on panel methods

Fig. 13. Moments M_x and M_y at the right wing root.

load cases. However, this is certainly no general rule and may be different for any other aircraft.

Focusing on the right side of the subsonic load envelopes (load cases 10071, 10072, 10077 and 10091), the corresponding operational point is flight speed VC, at sea level and with mass configuration M2 (BFDM) and M3. The maneuvers are a pull-up with $N_z = +9.0$ in combination with roll. Load case 10071 has a positive rate p (roll to the right), leading to a high positive torsional moment M_y at the wing root induced by the ailerons, while load case 10072 has a negative rate p (roll to the left), resulting in a high negative torsional moment M_y at the wing root. Load cases 10091 is similar to 10072 but for a different mass case (M3) while load case 10077 is similar to 10071 but with an accelerated roll (with $\dot{p}$ in opposite direction of p). So from this perspective, the results are plausible. However, the corresponding Mach number is very close to $Ma = 1.0$, see Fig. 12, making the VLM aerodynamics untrustworthy due to the proximity to the singularity at $Ma = 1.0$ from the Prandtl-Glauert transformation. Note that to avoid that singularity, the **AIC** matrix was calculated for $Ma = 0.9$ instead. Although the VLM based load envelopes identify the correct load cases, the method fails because the magnitude of the section loads is unreliable.

The right side of the supersonic load envelope (load cases 20295, 20096, 20301 and 20315) is defined by the same set of maneuvers, but at a higher flight speed VD, which corresponds to $Ma = 1.2$. Like before, the ZONA51 based load envelopes identify the correct load cases, but the method fails because the magnitude of the section loads is unreliable.

To give a broaded picture, Figs. 14a to 14d show the merged load envelopes (from both sub- and supersonic load cases) at four different monitoring stations. As a reference, Fig. 14a shows the bending moment M_x and the torsional moment M_y at the right wing root, which is basically a fusion of the data already given in Figs. 13a and 13b. As discussed before, the envelope of the CFD maneuver loads (black) is larger compared to the loads based on panel methods (gray), especially with regard to the corners. Moving to the monitoring stations at the mid and outer wing, given in Figs. 14b and 14c, the disagreement becomes more pronounced. Fig. 14d shows the shear forces in z- and y-direction F_z and F_y. While the agreement of the shear forces F_z is acceptable, there is a significant difference for the shear forces F_y. This physical difference can be explained by the strong vortices, which create not only lift but also a span-wise suction force acting on the front fuselage, which don't exist in the panel methods. Note that the shear forces F_y from the panel methods are not exactly zero because of inertia forces.

Although the convergence of the CFD solutions was very robust, about 1% of the load cases didn't converge. In a pragmatic

approach, these load cases were considered as not achievable / flyable and were excluded from the sizing presented in the next Section.

5. Structural optimization

In this Section, a structural sizing is performed to evaluate and illustrate the influence of the different loads obtained in the previous section in terms of required material thickness and structural mass. Therefor, the structural sizing is formulated as a structural optimization problem in MSC.Nastran SOL200 and using IPOPT [46], which is a gradient-based optimization algorithm for large scale nonlinear problems. The design variables of the FFD are the material thicknesses of the shell elements of the skin, spars and ribs and the cross section of the fuselage beam elements. Note that other parameters, such as stringer size or spacing, remain fixed. The parameters are changed per design field, where one design field is for example the area between two ribs and two spars. The FFD comprises 304 design fields, resulting in 304 design variables **x**. The objective $f(\mathbf{x})$ is to minimize the structural mass while the constraints **g** are satisfied. As constraint, the maximum allowable stress for a 2024 aluminum (3.1354, T3) with $\sigma_{\text{allow}} = \pm 270.0$ MPa (elastic deformation only) is evaluated. For simplicity only one material is used for the entire primary structure, for a more elaborated design, different materials such as 7075 aluminum or composite materials could be applied in selected areas. Also, buckling is not considered in this optimization but as explained in Section 2.2, actually there are stiffeners and stringers for all ribs, spars and the skin with a pre-selected size (e.g. with a stringer-skin-ration of $\approx$ 20-30% and 70-80% of the cross section of a panel) to prevent buckling. Side constraints are the minimum allowable skin thickness $t_{\text{min}} = 1.0$ mm and the minimum allowable height of the beam profile with $w_{\text{min}} = 100.0$ mm to avoid unrealistic designs. Note that the remaining dimensions of the beam profile are linked and scaled linearly, so that in essence the whole cross section of the beam element is changed.

In the previous Section, the loads are calculated as limit loads while the structure is also sized with ultimate loads, which equals 1.5 times the limit loads. The physical background is that plastic deformation may occur on a local level beyond limit load but failure of the primary, load carrying structure should not occur up to ultimate load. Some authors, like Watson [25], argue that with a limit load protection included in the EFCS, this factor could be relaxed (e.g. to 1.4) because exceeding limit load is less likely compared with an aircraft where the pilot is responsible for not exceeding the limit loads. In this work, the factor of 1.5 is considered in the allowable stresses. A bonus of the selected 2024 aluminum material is a comparably high maximum
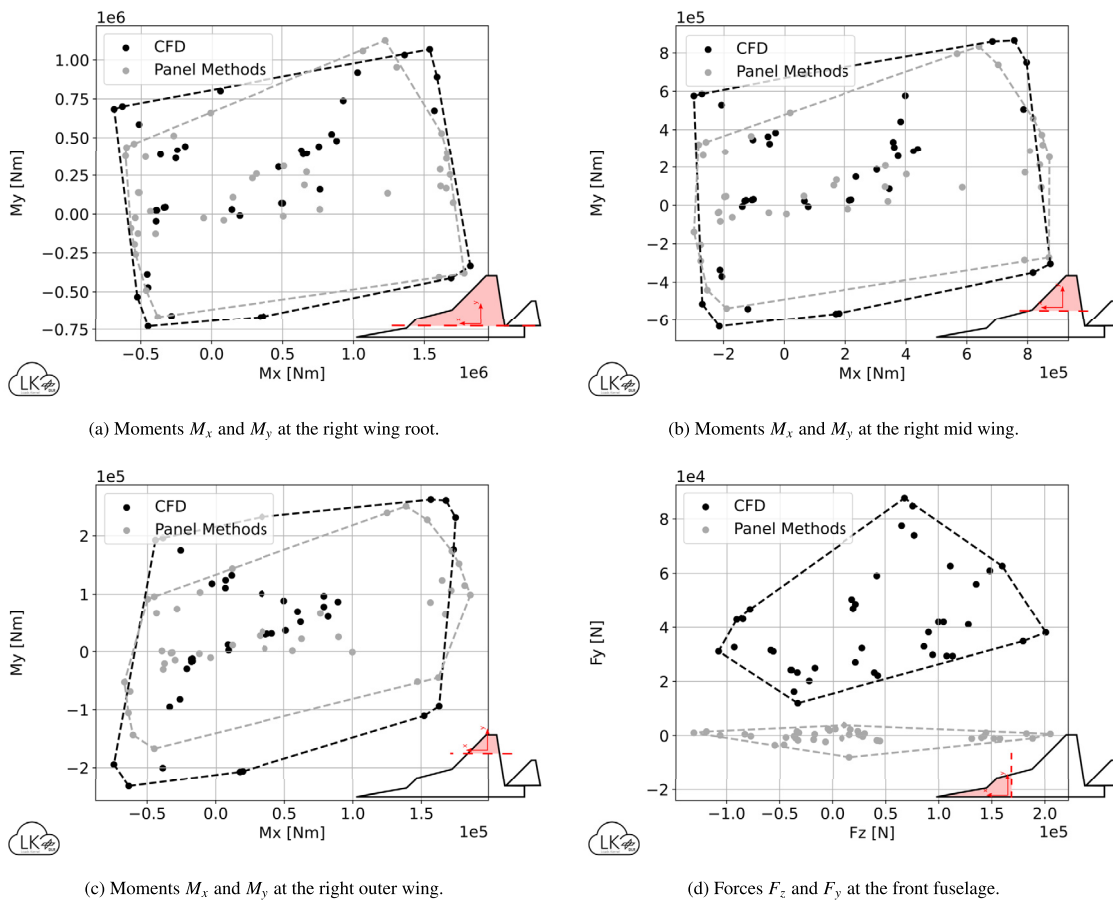
(a) Moments M_x and M_y at the right wing root.

(b) Moments M_x and M_y at the right mid wing.

(c) Moments M_x and M_y at the right outer wing.

(d) Forces F_z and F_y at the front fuselage.

Fig. 14. Comparing load envelopes from CFD and panel methods at different monitoring stations.

stress with $\sigma_{\max} = \pm 440.0$ MPa (fracture occurs), which means that the ultimate load criterion is automatically satisfied because 270 MPa $\cdot 1.5 = 405$ MPa, which is less than the maximum stress $\sigma_{\max}$.

The loads analysis and the structural optimization form an iterative process, because a change in structural mass influences the loads and vice versa. The mass history of the sizing loops is given in Fig. 15. In this case, mass convergence ($\Delta m \leq 1.0\%$) is achieved quickly after only three to four loops. The first three loops were performed with a previous configuration (FFD-A) and are given only for reference. With the present configuration (FFD-B), the previous results are used to perform a "warm start" for both the CFD and panel method based sizing. From Fig. 15 it is evident that the CFD based sizing leads to a higher structural net mass of ≈ 4.1 t compared to the panel method based sizing with only ≈ 3.3 t. Note that the results are strongly influenced by the selected minimum skin thickness, which is influenced strongly by practical considerations such as impact damage from debris during take-off and landing, so these results mark the lower end of the physical and technical possible.

The resulting material thickness is shown in Fig. 16. In many design fields, the minimum allowable skin thickness $t_{\min} = 1.0$ mm is sufficient, which is indicted by the yellow color. Looking at the lower and upper skin of the wing, a load path where the material thickness is increased is clearly visible between the front and rear spar, indicated by the orange and red colors. In the fuselage, the height of the cross section and, consequently, the second area moment and the ability to take bending loads increases so that the skin thickness decreases again. This load path is also reflected by the material thickness of the spars, where the middle spar reaches a maximum thickness of $t \approx 15.0$ mm at the wing root. In a sim-

ilar way, the material thickness of the HTP is increased between the two spars and the load path is continued into the rear fuselage. A significant difference between Fig. 16a and 16b can be seen in the front section towards the cockpit (design field with dark blue color) and with $t \approx 50.0$ mm, the skin thickness is actually out of the range of the color map. This local increase in material thickness can be explained by the much higher shear forces in y-direction, which were already identified in the previous section in Fig. 14d. The high suction force of the vortices acts on the fuselage, leading to high local stresses, which don't exist in the panel method based sizing. The physical difference is magnified by the fact that neither the cockpit nor the air intakes are modeled structurally, which would distribute the forces on multiple structural members and decrease the local stresses. Summing up, the optimization results look plausible from an engineering perspective. Note that, like most optimizer, IPOPT finds 'only' a local optimum, which is acceptable for this application. In case of strange and/or doubtful results, a possibility to increase the confidence in the solution could be to start the optimization from a different initial point.

6. Conclusion and outlook

Loads and aeroelastic models, comprising structures, detailed mass models and aerodynamics, are developed for a future fighter demonstrator (FFD). Comparing different aerodynamic methods, it becomes obvious that the panel methods are at their physical limit for fighter aircraft, indicating that CFD should be preferred over panel methods. A comprehensive maneuver loads analysis covering the whole flight envelope is performed with both CFD and panel methods. Although the load envelopes based on the VLM and
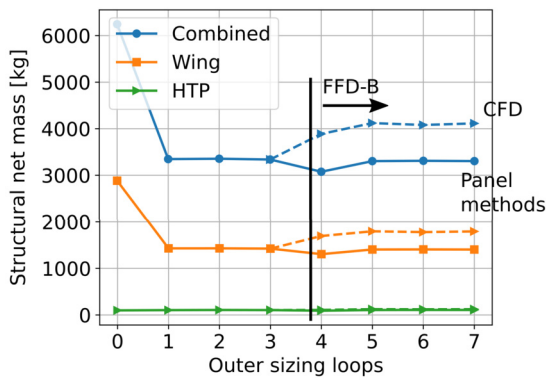
Fig. 15. Mass convergence of the FE model. Continuous line: panel methods, dashed line: CFD.
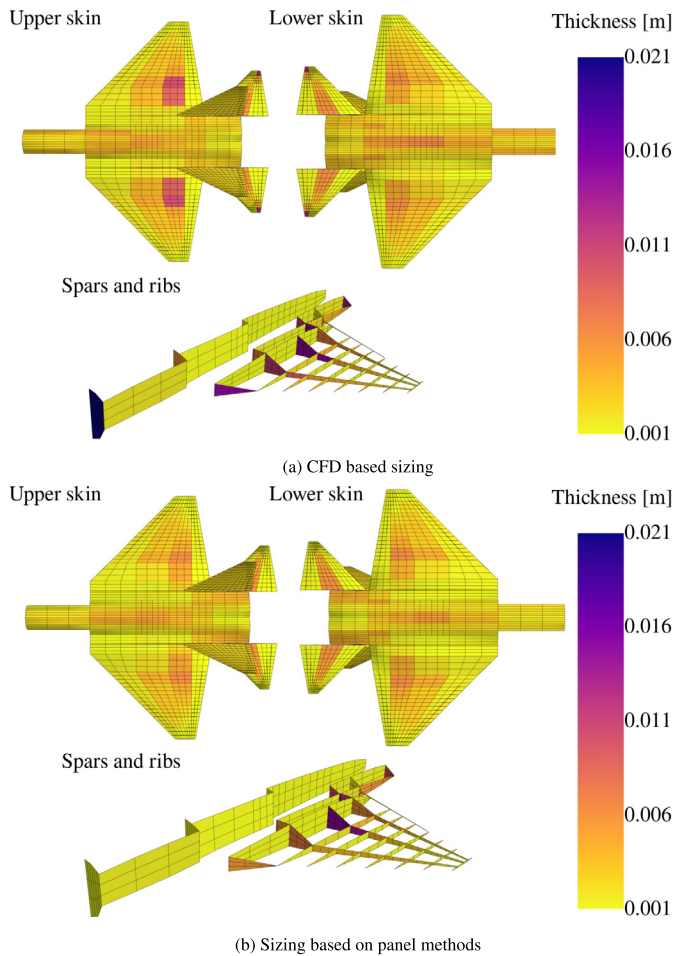

(a) CFD based sizing

(b) Sizing based on panel methods

Fig. 16. Resulting material thickness of the shell elements.

craft. Due to the linear approach, the deflected wing also stretches in span direction, which has a direct (although small) influence on the CFD solution. The same is true for the control surfaces, where the deflections are performed with the assumption of small angles. In addition, the control surface deflection is modeled in CFD using a deformed mesh approach, which could be replaced by a more sophisticated methodology based on chimera and/or sliding mesh techniques. Although the Euler solutions performed well in comparison with the RANS solutions, switching to RANS would add even more physical effects. For example, viscosity has not only an influence on drag (typically not so important for loads), but also influences the position and strength of compression shocks. For the evaluation and the identification of dimensioning load cases, two-dimensional load envelopes were used at selected monitoring stations. More detailed analyses could be performed using a more elaborate method proposed by [47,48], which is based on finite elements and calculates the failure indices for each element for each load case. The highest failure index of an element then identifies the critical load case. Finally, as the aeroelastic models are now available, further aeroelastic analyses can be performed, for example with respect to control surface effectiveness or flutter and/or with additional mass configurations including external payloads or fuel tanks attached to the wing.

Declaration of competing interest

The authors declare that they have no known competing financial interests or personal relationships that could have appeared to influence the work reported in this paper.

Data availability

The authors do not have permission to share data.

References

[1] A. Voß, T. Klimmek, Aeroelastic Modeling, Loads Analysis and Structural Design of a Fighter Aircraft, International Council of the Aeronautical Sciences, Stockholm, Sweden, 2022.

[2] A. Mancini, J. Zamboni, E. Moerland, A knowledge-based methodology for the initiation of military aircraft configurations, in: American Institute of Aeronautics and Astronautics, Virtual Event, 2021, https://arc.aiaa.org/doi/10.2514/6.2021-2789.

[3] M. Stradtner, C.M. Liersch, P. Löchert, Multi-Fidelity Aerodynamic Data Set Generation for Early Aircraft Design Phases, NATO Science and Technology Organization, 2022.

[4] M. Alder, E. Moerland, J. Jepsen, B. Nagel, Recent advances in establishing a common language for aircraft design with CPACS, Bordeaux, France, https://elib.dlr.de/134341/.

[5] M. Schulze, T. Klimmek, F. Torrigiani, T.F. Wunderlich, Aeroelastic design of the oLAF reference aircraft configuration, Bremen (virtual), https://elib.dlr.de/143642/.

[6] T. Klimmek, S. Dähne, B. Fröhler, J. Hartmann, D. Kohlgrüber, M. Petsch, M. Schulze, A. Schuster, Ö. Süelözgen, High-fidelity-based MDO: a closer look at the selected sub-processes overall aircraft design synthesis, loads analysis, and structural optimization, virtual event, https://elib.dlr.de/137392/.

[7] V. Handojo, Contribution to Load Alleviation in Aircraft Pre-design and Its Influence on Structural Mass and Fatigue, Dissertation, TU Berlin, Berlin, Germany, 2020.

[8] K. Sinha, T. Klimmek, M. Schulze, V. Handojo, Loads analysis and structural optimization of a high aspect ratio, composite wing aircraft, CEAS Aeronaut. J. 12 (2021) 233–243, https://link.springer.com/10.1007/s13272-021-00494-x.

[9] A. Voß, Design and Structural Optimization of a Flying Wing of Low Aspect Ratio Based on Flight Loads, Dissertation, Technische Universität Berlin, Berlin, Germany, 2020.

[10] T. Hecken, S. Cumnuantip, T. Klimmek, Structural design of heavy-lift unmanned cargo drones in low altitudes, in: J.C. Dauer (Ed.), Automated Low-Altitude Air Delivery, Springer International Publishing, Cham, 2022, pp. 159–183, https://link.springer.com/10.1007/978-3-030-83144-8_7.

[11] A. Voß, V. Handojo, C. Weiser, S. Niemann, Preparation of loads and aeroelastic analyses of a high altitude, long endurance, solar electric aircraft, CEAS and 3AF, Bordeaux, France, https://elib.dlr.de/133496/, 2020.

ZONA51 identify the correct load cases, the methods fail because the magnitude of the section loads is unreliable, showing the necessity of a maneuver loads analysis using CFD in the preliminary design for such fighter configuration. As mentioned before, this is a heavy burden but doable as of today. To illustrate the impact on the structural design, a structural sizing is performed, leading to a heavier structural net mass of $\approx 4.1\,t$ for the CFD based approach compared to the panel method based sizing with only $\approx 3.3\,t$.

Although with the use of CFD, many physical details are added to the maneuver loads analysis, several simplifications were made in this study. For example, the structure is modeled geometrically linear, which is justified for stiff configurations such as fighter air-

[12] A. Voß, V. Handojo, C. Weiser, S. Niemann, Results from loads and aeroelastic analyses of a high altitude, long endurance, solar electric aircraft, J. Aeroelast. Struct. Dyn. 9 (2022) 1–22, https://elib.dlr.de/147956/.

[13] W. Stauffer, J. Lewolt, F. Hoblit, Application of advanced methods to the determination of design loads of the Lockheed L-1011 TriStar, AIAA J. (1972), http://arc.aiaa.org/doi/abs/10.2514/6.1972-775.

[14] W.A. Stauffer, J.G. Lewolt, F.M. Hoblit, Application of advanced methods to design loads determination for the L-1011 transport, J. Aircr. 10 (1973) 449–458, https://doi.org/10.2514/3.60248.

[15] R. D'Vari, M. Baker, Aeroelastic loads and sensitivity analysis for structural loads optimization, J. Aircr. 36 (1999) 156–166, https://doi.org/10.2514/2.2421.

[16] T. Kier, J. Hofstee, VarLoads - Eine Simulationsumgebung zur Lastenberechnung eines voll flexiblen, freifliegenden Flugzeugs, in: Deutscher Luft- und Raumfahrtkongress, Dresden, 2004.

[17] T. Kier, G. Looye, M. Scharpenberg, M. Reijerkerk, Process, methods and tools for flexible aircraft flight dynamics model integration, in: International Forum on Aeroelasticity and Structural Dynamics, Stockholm, Sweden, 2007, http://elib.dlr.de/55663/.

[18] M. Scharpenberg, T. Kier, L. Taules, Considerations on an integral flight physics model with application to loads analysis, in: SAE International, 2011, http://papers.sae.org/2011-01-2767/.

[19] A. Voß, Loads Kernel User Guide, Technical Report DLR-IB-AE-GO-2020-136, Institut für Aeroelastik, Deutsches Zentrum für Luft- und Raumfahrt, Göttingen, Germany, 2021, https://elib.dlr.de/140268/.

[20] A. Voß, An Implementation of the Vortex Lattice and the Doublet Lattice Method, Technical Report DLR-IB-AE-GO-2020-137, Institut für Aeroelastik, Deutsches Zentrum für Luft- und Raumfahrt, Göttingen, Germany, 2020, https://elib.dlr.de/136536/.

[21] Multiple authors, Loads and requirements for military aircraft, in: Proceedings of the AGARD Structures and Materials Panel Meeting on "Loads and Requirements for Military Aircraft", AGARD Report 815, Florence, Italy, 1997.

[22] M. authors, Design Loads for Future Aircraft, Technical Report RTO-TR-045, NATO Research and Technology Organisation, 2002.

[23] C. Petiau, Evolution de la philosophie des charges de dimensionnement des avions militaires, AGARD, Florence, Italy, 1996.

[24] M. Neubauer, G. Gunther, Aircraft Loads, NATO RTO, Sofia, Bulgaria, 2000, https://apps.dtic.mil/sti/citations/ADP010772.

[25] G.J. Watson, Eurofighter 2000 Structural Design Criteria and Design Loading Assumptions, AGARD, Florence, Italy, 1996.

[26] W.G. Luber, J. Becker, O. Sensburg, The Impact of Dynamic Loads on the Design of Military Aircraft, AGARD, Florence, Italy, 1996.

[27] J. Molkenthin, Determination and Verfication of Operational Maneuver Parameters and Time Histories, AGARD, Florence, Italy, 1996.

[28] H. Struck, C. Perron, Flight Loads Derived from Operational Maneuvers, AGARD, Florence, Italy, 1996.

[29] MIL-A-8860B, Airplane Strength and Rigidity General Specifications, 1987.

[30] MIL-A-8861B, Airplane Strength and Rigidity Flight Loads, 1986.

[31] European Aviation Safety Agency (Ed.), Certification specifications for large aeroplanes CS-25, amendment 16 edition, https://www.easa.europa.eu/certification-specifications/cs-25-large-aeroplanes, 2015.

[32] T. Klimmek, Parameterization of topology and geometry for the multidisciplinary optimization of wing structures, in: CEAS 2009 - European Air and Space Conference, Council of European Aerospace Societies, Manchester, United Kingdom, 2009.

[33] M. Siggel, J. Kleinert, T. Stollenwerk, R. Maierl, TiGL: an open source computational geometry library for parametric aircraft design, Math. Comput. Sci. 13 (2019) 367–389, https://doi.org/10.1007/s11786-019-00401-y.

[34] F. Lin, W.T. Hewitt, Expressing Coons-Gordon surfaces as nurbs, Comput. Aided Des. 26 (1994) 145–155, https://www.sciencedirect.com/science/article/pii/0010448594900353.

[35] P.-C. Chen, D.D. Liu, A harmonic gradient method for unsteady supersonic flow calculations, J. Aircr. 22 (1985) 371–379, https://doi.org/10.2514/3.45134.

[36] D.D. Liu, D.K. James, P.C. Chen, A.S. Pototzky, Further studies of harmonic gradient method for supersonic aeroelastic applications, J. Aircr. 28 (1991) 598–605, https://doi.org/10.2514/3.46070.

[37] B. Probert, Aspects of Wing Design for Transonic and Supersonic Combat Aircraft, NATO RTO, Rhode-Saint-Gentèse, Belgium, 1998.

[38] D. Schwamborn, T. Gerhold, R. Heinrich, The DLR tau-code: recent applications in research and industry, in: European Conference on Computational Fluid Dynamics, 2006.

[39] T.D. Economon, F. Palacios, S.R. Copeland, T.W. Lukaczyk, J.J. Alonso, SU2: an open-source suite for multiphysics simulation and design, AIAA J. 54 (2016) 828–846, https://arc.aiaa.org/doi/10.2514/1.J053813.

[40] Siemens AG, Simcenter 3D — Siemens Software, https://www.plm.automation.siemens.com/global/en/products/simcenter/simcenter-3d.html, 2022.

[41] CentaurSoft, CENTAUR software from CentaurSoft - mesh (grid) generation for CFD and computational simulations, https://www.centaursoft.com/, 2022.

[42] A.J. Banko, J.K. Eaton, A frame-invariant definition of the Q-criterion, in: Stanford University Center for Turbulence Research Annual Research Briefs, 2019, pp. 181–194.

[43] M.S. Chong, A.E. Perry, B.J. Cantwell, A general classification of three-dimensional flow fields, Phys. Fluids A, Fluid Dyn. 2 (1990) 765–777, https://aip.scitation.org/doi/10.1063/1.857730.

[44] K.G. Pratt, W.G. Walker, A Revised Gust-Load Formula and a Re-evaluation of V-G Data Taken on Civil Transport Airplanes from 1933 to 1950, Technical Report NACA-TR-1206, National Advisory Committee for Aeronautics, Langley Aeronautical Lab., Langley Field, VA, 1953.

[45] K.G. Pratt, A Revised Formula for the Calculation of Gust Loads, Technical Note TN 2964, National Advisory Committee for Aeronautics, Langley Aeronautical Lab., Langley Field, VA, 1953, http://ntrs.nasa.gov/search.jsp?R=19930084025.

[46] A. Wächter, L.T. Biegler, On the implementation of an interior-point filter line-search algorithm for large-scale nonlinear programming, Math. Program. 106 (2006) 25–57, https://doi.org/10.1007/s10107-004-0559-y.

[47] K. Bramsiepe, A. Voß, M. Herberhold, Aeroelastic Load Selection Based on Failure Indices on Finite Element Level, Deutsche Gesellschaft für Luft- und Raumfahrt - Lilienthal-Oberth e.V., Bremen, 2021, https://elib.dlr.de/144540/.

[48] M. Herberhold, A. Voß, K. Bramsiepe, Identifizierung dimensionierender Lastfälle auf Ebene finiter Elemente an einer Nurflügelstruktur im Vergleich zur Schnittlastmethode, Deutsche Gesellschaft für Luft- und Raumfahrt - Lilienthal-Oberth e.V., Bremen, 2021, https://elib.dlr.de/143155/.